Relationship between cusp-region ion outflows and east-west magnetic field fluctuations in Southern and Northern Hemispheres

S. M. Hatch[1*], T. Moretto[1], K. A. Lynch[2], K. M. Laundal[1], J. W. Gjerloev[1,3], E. J. Lund[4]

[1]Birkeland Center for Space Science, University of Bergen, Bergen, Norway
[2]Department of Physics and Astronomy, Dartmouth College, Hanover, New Hampshire, USA.
[4]The Johns Hopkins University Applied Physics Laboratory, Laurel, Maryland, USA
[4]Space Science Center, University of New Hampshire, Durham, New Hampshire, USA

Key Points:

- Summer/equinox outflows and east-west field fluctuations are highly correlated ($r > .92$).
- Winter outflows are poorer in oxygen and less correlated with field fluctuations ($r > .75$).
- Power indices 0.7–1.2 characterize statistical relationship between outflows and field fluctuations

*Department of Physics and Technology, Allégaten 55, N-5007 Bergen, Norway

Corresponding author: S. M. Hatch, Spencer.Hatch@uib.no

Abstract

A number of interdependent conditions and processes contribute to ionospheric-origin energetic ion outflows. Due to these interdependences and the associated observational challenges, energetic ion outflows remain a poorly understood facet of atmosphere-ionosphere-magnetosphere coupling. Here we demonstrate the relationship between east-west magnetic field fluctuations ($\Delta B_{\rm EW}$) and energetic outflows in the magnetosphere-ionosphere transition region. We use dayside cusp-region FAST satellite observations made at apogee ($\sim$4200-km altitude) near fall equinox and solstices in both hemispheres to derive statistical relationships between ion upflow and ($\Delta B_{\rm EW}$) spectral power as a function of spacecraft-frame frequency bands between 0 and 4 Hz. Identification of ionospheric-origin energetic ion upflows is automated, and the spectral power P_{EW} in each frequency band is obtained via integration of $\Delta B_{\rm EW}$ power spectral density. Derived relationships are of the form $J_{\parallel,i} = J_{0,i} P_{EW}^{\gamma}$ for upward ion flux $J_{\parallel,i}$ at 130-km altitude. The highest correlation coefficients are obtained for spacecraft-frame frequencies $\sim$0.1–0.5 Hz. Summer solstice and fall equinox observations yield power law indices $\gamma \simeq 0.9$–1.3 and correlation coefficients $r \geq 0.92$, while winter solstice observations yield $\gamma \simeq 0.4$–0.8 with $r \gtrsim 0.8$. Mass spectrometer observations reveal that the oxygen/hydrogen ion composition ratio near summer solstice is much greater than the corresponding ratio near winter. These results thus reinforce the importance of ion composition in any outflow model. If observed $\Delta B_{\rm EW}$ variations are purely spatial and not temporal, we show that spacecraft-frame frequencies $\sim$0.1–0.5 Hz correspond to perpendicular spatial scales of several to tens of kilometers.

1 Introduction

Energetic ion outflow is a complex phenomenon within the coupled atmosphere-ionosphere-magnetosphere system that can occur via a number of multi-stage pathways. These stages depend on both large-scale system properties such as levels of insolation, geomagnetic and substorm activity, interplanetary magnetic field strength and orientation, and the solar wind (Yau & André, 1997; Su et al., 1999; Wilson et al., 2004; Moore & Horwitz, 2007; Howarth & Yau, 2008; Peterson et al., 2008; Welling et al., 2015; Lee et al., 2016) and a host of more localized processes and conditions such as ambipolar electric fields, thermospheric neutral density enhancements, electron density, soft (<1 keV) electron precipitation, resonant and/or stochastic wave-particle interactions, polar cap

patches, and Joule heating (Norqvist et al., 1998; Strangeway et al., 2005; Burchill et al., 2010; Kervalishvili & Lühr, 2013; Q.-H. Zhang et al., 2016). Any particular instance of energetic ion outflow therefore represents interplay between a variable number of processes and conditions, which themselves vary over spatial scales ranging from tens to thousands of kilometers and over time scales ranging from seconds to years (Horwitz & Zeng, 2009; Varney et al., 2016). Thus complete monitoring of the energetic ion outflow process represents an enormous observational challenge, requiring in situ wave and particle observations extending from the base of the thermosphere/ionosphere through several thousand kilometers altitude.

Previous works (Strangeway et al., 2005; Zheng et al., 2005) have illustrated how covariance of putative drivers of ion upflow complicate the interpretation of the role of any particular driver. These authors nevertheless show that drivers such as electron precipitation and Poynting flux are directly correlated with energetic ion upflow. In particular Strangeway et al. (2005), hereafter S05, reported a correlation coefficient $r = 0.721$ between average upward ion flux $\langle J_{\parallel,\mathrm{up}} \rangle$ composed predominantly of oxygen and average "DC" (i.e., spacecraft-frame frequencies f_{sc} =0–0.125 Hz) Poynting flux $\langle S_{DC} \rangle$ based on measurements made during 33 Fast Auroral SnapshoT (FAST) satellite passes of the Northern Hemisphere (NH) dayside cusp region near apogee (∼4200-km altitude) in local fall equinox. Using the same 33 FAST dayside passes, Brambles et al. (2011), hereafter B11, reported a correlation coefficient $r = 0.795$ between $\langle J_{\parallel,\mathrm{up}} \rangle$ and average "AC" (f_{sc} =0.125–0.5 Hz) Poynting flux $\langle S_{AC} \rangle$. From these observations S05 and B11 respectively derived an empirical relationship between $\langle J_{\parallel,\mathrm{up}} \rangle$ and $\langle S_{DC} \rangle$, and between $\langle J_{\parallel,\mathrm{up}} \rangle$ and $\langle S_{AC} \rangle$.

A likely physical explanation for the correlation between upward ion flux and Poynting flux at frequencies between 0.125 Hz and 0.5 Hz at FAST altitudes is that this spacecraft-frame frequency band is associated with Alfvén waves (Brambles et al., 2011; B. Zhang et al., 2014; Hatch et al., 2017). Alfvén waves are strongly associated with and can directly drive ion outflow (Chaston et al., 2006, 2007). Observational and theoretical studies show that Alfvén wave magnetic field fluctuations are primarily oriented east-west (Stasiewicz et al., 2000; Chaston et al., 2003).

These empirical relationships, along with a similar set of relationships derived by Zheng et al. (2005) from 37 Polar satellite passes of the dayside Southern Hemisphere

(SH), have either been employed directly (Moore et al., 2007; Brambles et al., 2010, 2011) or otherwise served as points of reference in ion outflow simulations and theoretical works (Horwitz & Zeng, 2009; Moore & Khazanov, 2010; Brambles et al., 2011; Varney et al., 2016). These works nonetheless all express a need for additional observational studies to validate and expand these empirical relationships. Such studies have largely not been performed, due at least in part to a lack of applicable data sets (i.e., simultaneous electric field, magnetic field, and ion distribution measurements). There are furthermore no studies demonstrating how these statistical relationships might vary with season, local time, or interplanetary magnetic field conditions. There has resultantly been only limited progress in understanding the fundamental causes and processes of ionospheric-origin ion up/outflows during the past decade (Horwitz & Zeng, 2009; Varney et al., 2016).

In this study we consider the relationship between cusp-region upward ion fluxes and east-west magnetic field perturbations ΔB_{EW} in nearly arbitrary frequency bands, in both hemispheres during winter and summer. We also show that ion composition is likely an important factor in predicting energetic outflow fluxes. In Section 2 we describe FAST satellite ion and magnetic field (B-field) measurements and how we process these quantities to calculate average upward ion fluxes and east-west B-field fluctuations as a function of spacecraft-frame frequency band. We apply our methodology to the FAST observations that S05 and B11 considered, and compare our results to theirs. In Section 3 we use our methodology, together with four different groups of FAST observations made between December 1996 and January 1999, to obtain statistical relationships between average upward ion flux and ΔB_{EW} for nearly arbitrary spacecraft-frame frequencies between 0 Hz and 4 Hz. In Section 4 we discuss and summarize the results in Section 3, including how our methodology could be applied to current satellite missions; we discuss the role of ion composition in these as well as previous results; and we show that if we assume observed field perturbations are spatial rather than temporal, the perpendicular length scales associated with outflow at FAST apogee are of order several to a few tens of kilometers.

2 Data Set and Methodology

Launched into a polar orbit on August 21, 1996, the FAST satellite covered the range of altitudes between approximately 350 km and 4180 km, covering all magnetic local time (MLT) sectors every ∼3 months due to the 83° inclination of the orbit (Carlson et al.,

Table 1. Groups of FAST orbits used in this study.

Group	Section	Time period	Hemisphere	Local Season	Approach[a]	N Orbits
1	3.1	Sep 23–26 1998[b]	Northern	Fall	Poleward	33
2	3.2	Dec 30 1996 to Jan 7 1997	Northern	Winter	Equatorward	38
3	3.3	Jan 8–15 1999	Southern	Summer	Poleward	32
4	3.4	May 24 to Jun 5 1998	Southern	Late Fall	Poleward	29

[a]FAST satellite direction of approach to the cusp region.

[b]The group of 33 orbits used by S05 and B11.

2001). The FAST scientific payload included a suite of instruments capable of measuring in situ magnetic and electric fields, two-dimensional electron and ion pitch-angle distributions, and three-dimensional distributions of select ion species (Carlson et al., 2001; Ergun et al., 2001; Klumpar et al., 2001). Level 2 particle measurements are available for the duration of the FAST mission (ended in April 2009); Level 2 magnetic field measurements are available through October 2002 (`https://cdaweb.sci.gsfc.nasa.gov/index.html/`).

We use Level 1 FAST fluxgate magnetometer B-field measurements and ion electrostatic analyzer (IESA) measurements of ion pitch-angle distributions, which are obtained through the SDT software package (`http://sprg.ssl.berkeley.edu/~sdt/SdtReleases.html`).

Table 1 summarizes the four groups of FAST orbits that are used in this study. The first consists of the group of 33 NH orbits during September 1998 considered by S05 and B11. The second consists of NH observations during local winter, and the third and fourth consist of SH observations during local summer and local fall, respectively. The latter three groups of orbits were selected based on the following criteria, which mimick the characteristics of the 33 orbits used by S05 and B11:

1. Availability of ion and B-field measurements over magnetic latitudes (MLats) between 60° and 87° in the NH (-87° to -60° in the SH) and over dayside magnetic local times (MLTs);

2. Continuous ion and B-field measurements at altitudes between 3800 km and FAST apogee;
3. Satellite trajectory on the dayside that is primarily aligned with the noon-midnight meridian (as opposed to being aligned with, e.g., the dawn-dusk meridian; see Figure 1a).

MLat and MLT are defined at a reference height $h_r = 130$ km in the Modified Apex coordinate system (hereafter MA_{130}) (Richmond, 1995; Laundal & Richmond, 2016), which we obtain from the `apexpy` Python package (van der Meeren et al., 2018). In our experience, inclusion of FAST observations made under conditions not meeting requirements (1)–(3) renders the intercomparison of analysis results from each orbit group difficult or impossible. In particular relaxing the second and third requirements leads to additional sources of uncertainty/Doppler shifting of the frequencies of field measurements, as well as difference in frames of reference between FAST and ionospheric upflows that lead to sometimes overwhelming spacecraft ram ion signatures in IESA measurements. (See Heelis & Hanson, 1998; Moore et al., 1998, for some discussion of ram ions.) Thus these requirements are imposed on orbit groups 2–4 in Table 1 to facilitate comparison with Group 1 observations, whose orbit characteristics are the basis of these requirements.

2.1 Ion measurements and upflow identification algorithm

The IESA sampled full two-dimensional ion pitch-angle distributions at cadences between approximately 0.4 Hz and 13 Hz, depending on the mode of operation. Figure 1a shows an example pitch-angle spectrogram derived from IESA ion measurements on Sep. 25, 1998 during FAST orbit 8276, which is the same orbit represented in Figures 1 and 2 of S05. Two ion populations are visible: (i) an isotropic (i.e., covering all pitch angles) magnetospheric-origin population with mirror points below the altitude of FAST, appearing between ∼00:04:40 and 00:07:50 UT; (ii) an ionospheric-origin intense upflowing ion population appearing between ∼00:04:40 and 00:13:30 UT, corresponding to energies between 4 and 500 eV and anti-earthward pitch angles $90° < \theta < 270°$. In Figure 1a the ionospheric-origin population is superimposed over the isotropic magnetospheric-origin population.

Figure 1b, which is the "upward ion" energy-time spectrogram that results from averaging over anti-earthward pitch angles, shows that the average differential energy

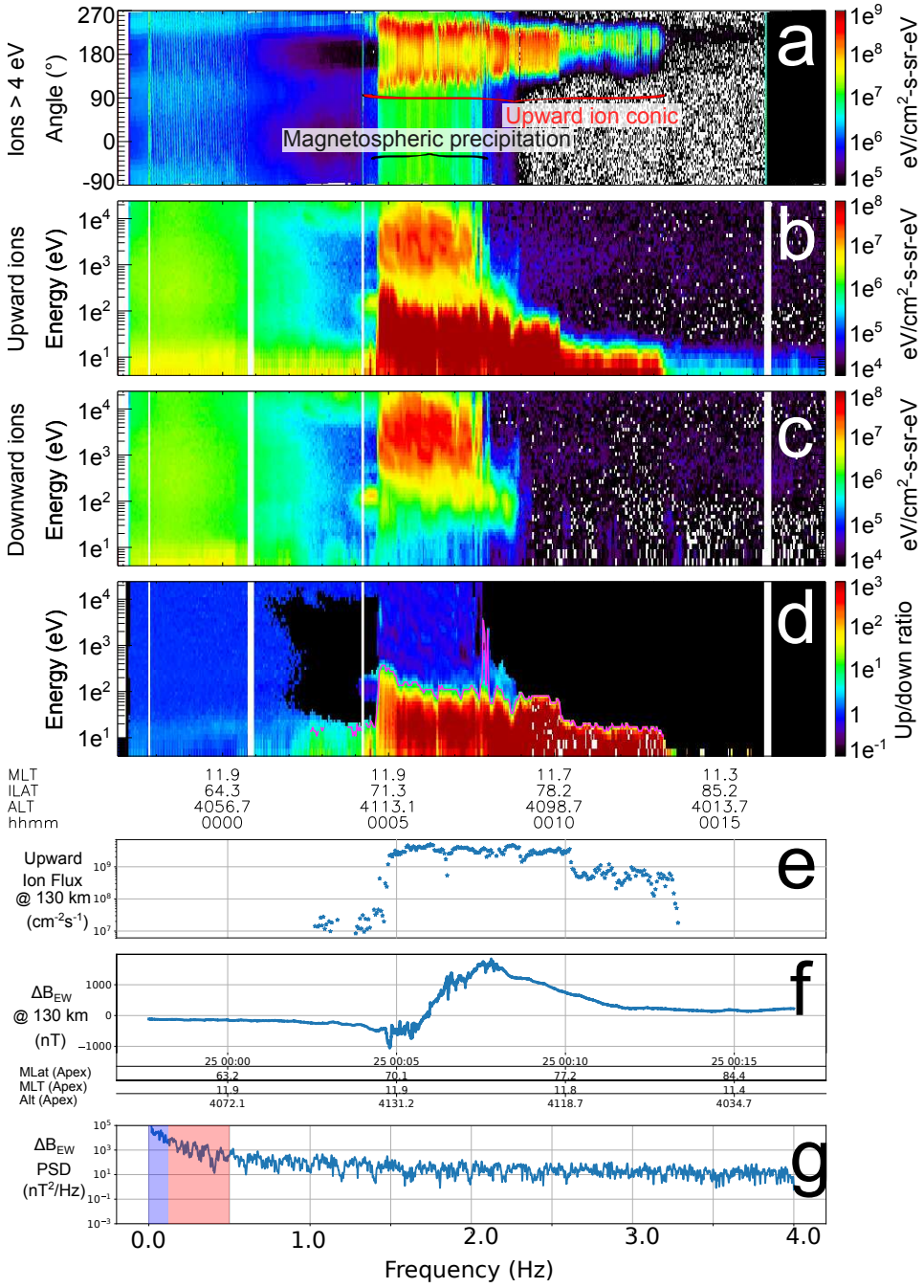

Figure 1. Ion and B-field quantities derived from FAST observations on September 25, 1998 in the Northern Hemisphere. (a) Pitch-angle spectrogram. (b) Energy spectrogram of anti-earthward ("upward") ions. (c) Energy spectrogram of earthward ("downward") ions. (d) Ratio of upward and downward spectrograms in Figures 1b and 1c. (e) Upward ion energy flux after mapping to 130-km altitude. (f) ΔB_{EW} after mapping to 130-km altitude. (g) Power spectral density estimate of ΔB_{EW} time series in Figure 1f. The spacecraft-frame frequency ranges termed "DC" (0–0.125 Hz) and "AC" (0.125–0.5 Hz) by S05 and B11 are highlighted in orange and blue, respectively, in Figure 1g. To avoid spuriously identifying background noise as upflow, for all energy bins in Figure 1b with upward differential energy fluxes $dJ_E/dE < 5 \times 10^5$ eV/cm^2-s-sr-eV the corresponding up/down ratio is set to zero in Figure 1d and in the upflow identification algorithm.

fluxes of the lower-energy, ionospheric-origin ion population are intense ($dJ_E/dE \gtrsim 10^8$ eV/cm^2-s-sr-eV). This ionospheric population does not appear in the "downward ion" spectrogram (Figure 1c), which is the ion energy-time spectrogram that results from averaging over all earthward pitch angles $|\theta| < 90°$.

We wish to exclude the contribution from magnetospheric ions to the calculated ionospherically sourced upward ion flux. To achieve this, S05 and B11 manually inspected the ion energy spectrogram from each cusp pass and visually determined a cutoff energy. They then integrated the observed ion distributions up to this cutoff energy and over all pitch angles.

Attempting to exactly reproduce the results of S05 and B11 is difficult because they do not state the ion cutoff energies that were used for each orbit. We have alternatively developed the following algorithm for identification of the appropriate upper bound on ion energy.

1. For each point in time, average particle counts in each energy-angle bin over all anti-earthward pitch angles to obtain an "upward ion" energy spectrogram (e.g., Figure 1b). Also average particle counts over all earthward pitch angles to obtain a "downward ion" energy spectrogram (e.g., Figure 1c).
2. Divide the upward ion spectrogram by the downward ion spectrogram to obtain an "up/down ratio" spectrogram (Figure 1d).
3. To avoid noise, set the up/down ratio to zero for all energy bins with upward differential energy flux $dJ_E/dE < 5 \times 10^5$ eV/cm^2-s-sr-eV.
4. Let the bin with the highest energy for which the up-down ratio is at least 5 be denoted E_{top}. If either (a) no bins have an up/down ratio of at least 5, or (b) less than 75% of energy bins below E_{top} have up/down ratios of at least 1, no upflow is present in this ion distribution.
5. If the ion distribution meets the foregoing criteria, obtain the upward ion flux $J_{\parallel,\mathrm{up}}$ by integrating the original two-dimensional ion distribution over all pitch angles and from the 4-eV lower limit of the IESA detector energy range up to E_{top}.

The pink line in Figure 1d indicates E_{top} as identified by this algorithm. The corresponding time series of $J_{\parallel,\mathrm{up}}$ is shown in Figure 1e. All $J_{\parallel,\mathrm{up}}$ are mapped to 130-km altitude (approximately the base of the F-region ionosphere) via multiplication by the

mapping factor $D = |\mathbf{d}_1 \times \mathbf{d}_2|$, where $\mathbf{d}_1$ and $\mathbf{d}_2$ are base vectors in the MA_{130} coordinate system. These vectors are defined such that D is the ratio of the main-field magnitudes at FAST and at the footpoint of the same field line (Richmond, 1995). Mapped values of $J_{\parallel,\mathrm{up}}$ are then averaged to obtain a single average upward ion flux.

2.2 Magnetic field measurements and PSD estimates

The fluxgate magnetometer sampled all three B-field components at rates between 8 Hz and 128 Hz, depending on the mode of operation. Despinning of B-field measurements is performed by the `ucla_mag_despin` routine that is included with SDT software, after which we subtract the International Geomagnetic Reference Field-12 main field model. The quantity $\Delta B_{EW} = \mathbf{e}_1 \cdot \mathbf{\Delta B}$ gives the (approximately) east-west component of the B-field perturbation vector $\mathbf{\Delta B}$, where $\mathbf{e}_1$ is an MA_{130} coordinate system base vector such that ΔB_{EW} is mapped to 130 km.

Via the multitaper method (Slepian, 1978; Thomson, 1982; Hatch & LaBelle, 2018), we estimate the power spectral density (PSD) of the portion of the time series that meets the MLat, MLT and altitude criteria given in section 2. We calculate the spectral power in a particular spacecraft-frame frequency band by integrating the PSD estimate over all frequencies within that band. For example, a ∼15-min time series of ΔB_{EW} is shown in Figure 1f, with the corresponding multitaper PSD estimate shown in Figure 1g. The spacecraft-frame frequency ranges termed "DC" (0–0.125 Hz) and "AC" (0.125–0.5 Hz) by S05 and B11 are respectively highlighted in blue and orange. Integration of the PSD estimate over DC and AC frequency bands thus defined yields spectral powers of 2.88×10^5 nT^2 and 6.67×10^2 nT^2, respectively.

2.3 Comparison with Strangeway et al. (2005) and Brambles et al. (2011)

In summary, the methodology of S05 and B11 is based on manual identification of an ion cutoff energy for each cusp pass and average Poynting flux calculated from time series of B-field and electric field measurements. In contrast, our methodology is based on automated identification of ion outflows for each cusp pass and a spectral representation of B-field measurements. We now compare analysis results using each methodology to determine whether our methodology, which excludes electric field measurements and uses frequency-domain (instead of time-domain) calculations of average B-field fluc-

tuations, yields correlation coefficients that are similar to those yielded by the S05 and B11 methodology.

Figure 2 presents the scatterplots of average upward ion flux versus ΔB_{EW} spectral power in DC and AC spacecraft-frame frequency bands (respectively Figures 2a and 2c) in the left-hand column from the same 33 orbits presented by S05 and B11, and the scatterplots of average upward ion flux versus Poynting flux in DC and AC frequency bands (respectively Figures 2b and 2d) presented by S05 and B11. Each panel also shows the best-fit line and fit parameters that result from performing a least-squares linear fit to the logarithm of the quantities shown on the x and y axes.

In the two panels showing "DC" field fluctuations (top row in Figure 2), the correlation coefficients are very similar ($r = 0.725$ and $r = 0.721$) while the slopes differ ($\gamma = 0.85$ and $\gamma = 1.265$ in Figures 2a and 2b, respectively). In the two panels showing "AC" field fluctuations (bottom row in Figure 2), the correlation coefficients are different ($r = 0.917$ and $r = 0.795$) while the slopes are almost identical ($\gamma = 1.20$ and $\gamma = 1.206$ in Figures 2c and 2d, respectively).

From the comparison of methodologies shown in Figure 2, we conclude that our methodology yields correlation values that are comparable to or higher than those resulting from the S05 and B11 methodologies. Our methodology makes apparent that electric field measurements are not necessary for determination of an empirical relationship between field fluctations and energetic ion outflow. We now apply our methodology to four groups of orbits to investigate the relationship between $J_{\parallel,\mathrm{up}}$ and ΔB_{EW} as a function of season, hemisphere, and frequency band.

3 Statistical Relationships Between Ion Outflow and ΔB_{EW}

The AC and DC frequency bands defined by S05 arose in connection with the interpolation and the series of decimations and smoothings that they applied to the time series of field measurements (Appendix A in Strangeway et al., 2005). In contrast the spectral method we use allows for analysis of an arbitrary frequency band, up to the frequency resolution of each PSD (typically less than 0.01 Hz).

In this section we perform the same type of correlation and fitting shown in Figure 2 for the 19,900 possible frequency bands between 0 Hz and 4 Hz with spectral resolution 0.02 Hz, for the four groups of orbits indicated in Table 1. We hypothesize that

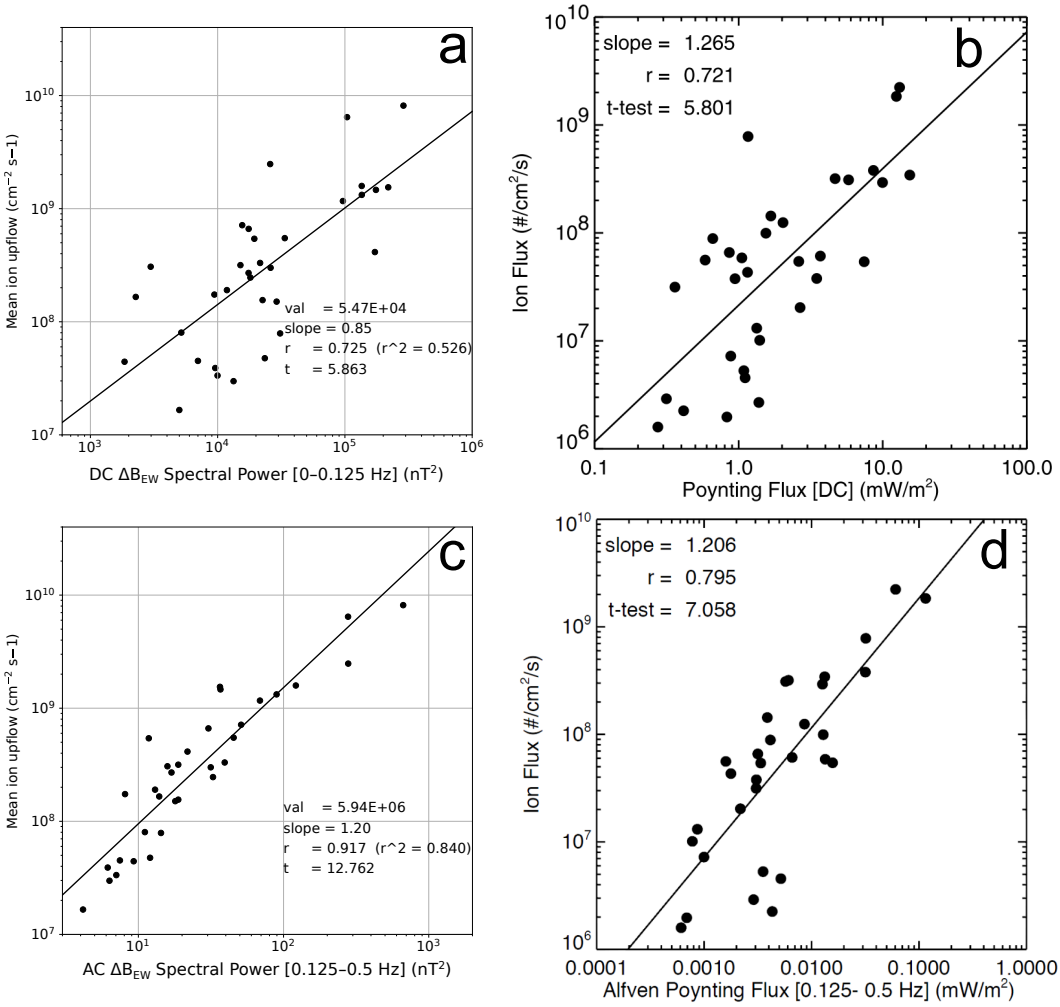

Figure 2. Scatterplots of average upward ion flux versus ΔB_{EW} spectral power (left column) and Poynting flux (right column) in DC (0–0.125 Hz; top row) and AC (0.125–0.5 Hz; bottom row) spacecraft-frame frequency bands for 33 NH cusp-region passes in September 1998. ΔB_{EW} spectral power in DC and AC frequency bands (left column) are calculated via the methodology described in section 2.2. Poynting flux in each frequency band (right column) is calculated via the methodology of S05. Each panel also shows the best-fit line and fit parameters described in section 2.3. Figure 2b was originally presented by S05 as Figure 5. Figure 2d was originally presented by B11 as their Figure S1. They are reproduced with permission from John Wiley and Sons and the American Association for the Advancement of Science, respectively.

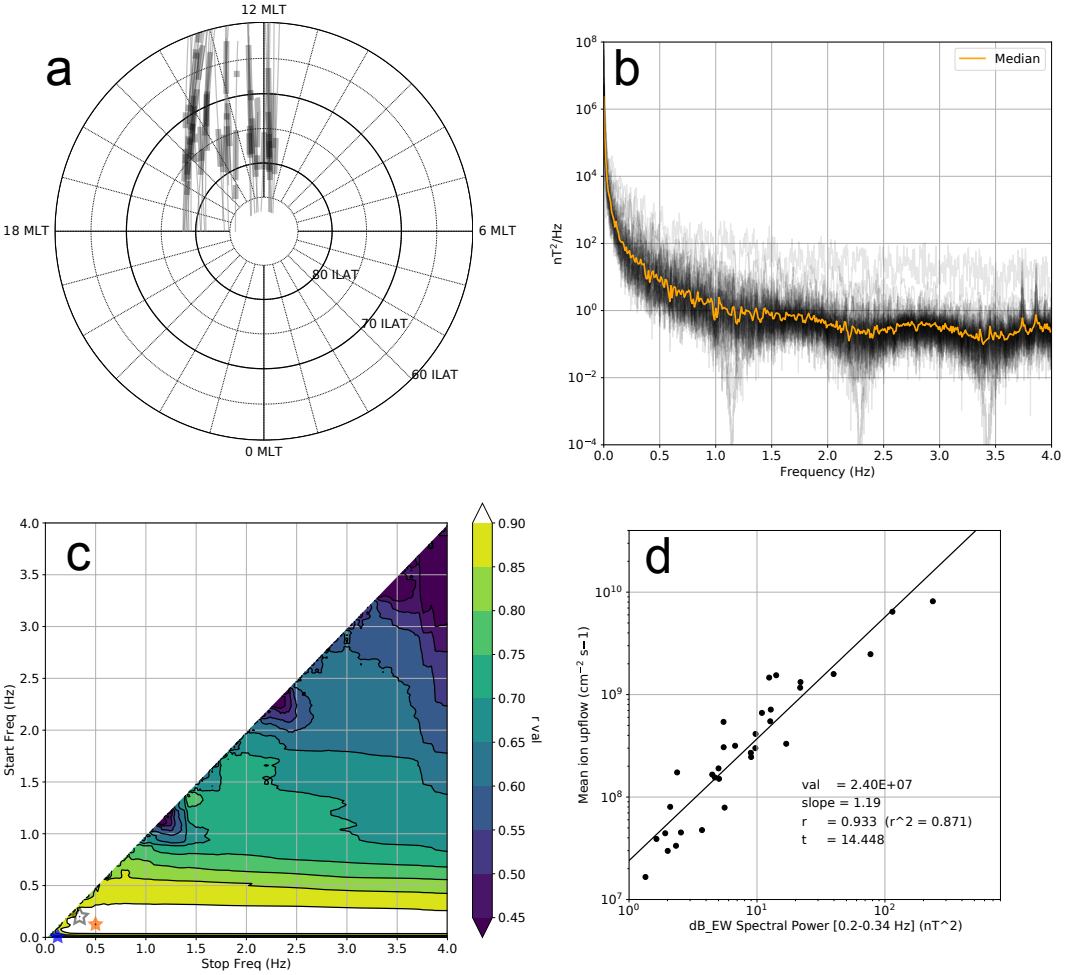

Figure 3. Ion and ΔB_{EW} statistics from 33 NH cusp-region passes during September 23–26, 1998. (a) Contributing portions of orbits, where thick lines indicate identified ion outflow. (b) Individual power spectral density (PSD) estimates of ΔB_{EW} time series (black transparent lines) and median PSD (orange line). (c) Correlation coefficient r of least-squares linear fit to the logarithm of average upward ion flux and logarithm of spectral power as a function of PSD start integration frequency (y axis) and stop integration frequency (x axis). (d) Least-squares linear fit for spacecraft-frame frequency band 0.2–0.34 Hz, which yields the highest least-squares correlation coefficient r in panel c. In panel c the S05 DC and AC frequency bands as well as highest-correlation frequency band are respectively indicated by blue, orange, and transparent black stars.

the inferred relationship between average ion outflow and B-field fluctuations varies as a function of season and hemisphere. To test this hypothesis we analyze each group of orbits separately.

3.1 Northern Hemisphere, September 1998 (Local Fall)

Figure 3 shows the results of analysis of 19,800 frequency bands between 0 Hz and 4 Hz for the 33 NH cusp-region passes considered by S05 and B11. Figure 3a shows the portion of each pass that meets the three criteria in section 2 (60–87° MLat, 6–18 MLT, and at or above 3800-km altitude), with thick lines indicating observations of ion outflow. Except during storms, the geomagnetic cusp is typically observed at 70° < MLat < 80° (Zhou et al., 2000; B. Zhang et al., 2013). The observation of ion outflows at MLat < 70° during several passes is therefore indicative of the geomagnetic storm that occurred during September 24–25, 1998.

Figure 3b shows the PSD estimate for each ΔB_{EW} time series as well as the median PSD (orange line). The median PSD ranges over nearly seven orders of magnitude, and decreases by roughly four orders of magnitude between 0 Hz and ∼0.2 Hz. (The two spikes that reach $\sim 10^{1.5}$ nT^2/Hz at ∼3.7 Hz and 3.9 Hz are artifacts related to the `ucla_mag_despin` routine, whereas the troughs at ∼1.1 Hz, 2.35 Hz, and 3.45 Hz are related to the recursive filter of the fluxgate magnetometer (Elphic et al., 2001). Similar artifacts are visible in the PSDs shown in Figures 4b, 5b, and 6b.)

Figure 3c displays the correlation coefficient r resulting from a least-squares linear fit to the logarithm of the average mapped upward ion flux and the logarithm of ΔB_{EW} spectral power within the frequency bands given by the x and y axes. The x axis gives the upper bound ("stop frequency") of the frequency band f_{top}, and the y axis gives the lower bound ("start frequency") of the frequency band f_{bot}. Each linear fit is of the form

$$\log_{10} J_{\parallel,i} = J_{0,i} + \gamma \log_{10} P_{EW}, \tag{1}$$

where $J_{\parallel,i}$ is the predicted upward ion flux after mapping to 130-km altitude, γ is the power-law index (Figure 3d), P_{EW} is the spectral power within the selected frequency band, and $J_{0,i}$ is the mapped upward ion flux (in cm^{-2}s^{-1}) for nominal spectral power $P_{EW} = 1$ nT^2.

As an aid in the interpretation of Figure 3c, we indicate with a blue star the DC frequency band 0–0.125 Hz defined by S05, corresponding to Figures 2a–b. (See also the DC frequency band shaded blue in Figure 1g.) We indicate with an orange star the AC frequency band 0.125–0.5 Hz defined by S05, corresponding to Figures 2c–d. (See also the AC frequency band shaded orange in Figure 1g.)

The highest correlation coefficients ($r \geq 0.9$) correspond to frequency bands such that 0.08 Hz $\lesssim f_{\text{bot}} \lesssim$ 0.3 Hz and $f_{\text{bot}} < f_{\text{top}} \lesssim$ 4 Hz. In particular the frequency band 0.2–0.34 Hz (indicated by the transparent black star in Figure 3c) yields the highest correlation coefficient $r = 0.933$, with a best-fit relationship $J_{\parallel,i} = 2.40 \times 10^7 P_{EW}^{1.19}$.

3.2 Northern Hemisphere, December 1996 (Local Winter)

Figure 4 shows the results of analysis of 19,800 frequency bands between 0 Hz and 4 Hz for 38 NH cusp-region passes occurring between December 30, 1996 and January 7, 1997, corresponding to local winter. The layout identical to that of Figure 3. Figure 4a shows that observed ion outflows are confined to MLat $\gtrsim 70°$ during these passes, with the majority observed at MLat $\gtrsim 75°$. Outflows at these latitudes are indicative of the geomagnetic quiescence that prevails throughout the nine-day period.

Figure 4b shows that the individual PSD estimates (transparent black lines) and median PSD (orange line) vary less overall than the PSD estimates shown in Figure 3b. The median PSD ranges over fewer than six orders of magnitude, decreasing by roughly two orders of magnitude over 0–0.2 Hz.

In Figure 4c, the highest correlation coefficients ($r \geq 0.75$) correspond to spacecraft-frame frequency bands such that 0.25 Hz$\leq f_{\text{bot}} \leq$0.7 Hz and 0.6 Hz$\leq f_{\text{top}} \leq$1.5 Hz. In particular the frequency band 0.64–0.66 Hz yields the highest correlation coefficient $r = 0.783$, with a best-fit relationship $J_{\parallel,i} = 1.35 \times 10^9 P_{EW}^{0.65}$.

3.3 Southern Hemisphere, January 1999 (Local Summer)

Figure 5 shows the results of analysis of 19,800 frequency bands between 0 Hz and 4 Hz for 32 SH cusp-region passes occurring between January 8 and January 15, 1999, corresponding to local summer. The layout is identical to that of Figure 3. Figure 5a shows that ion outflows are mostly observed at MLat $\gtrsim 70°$ during these passes. The

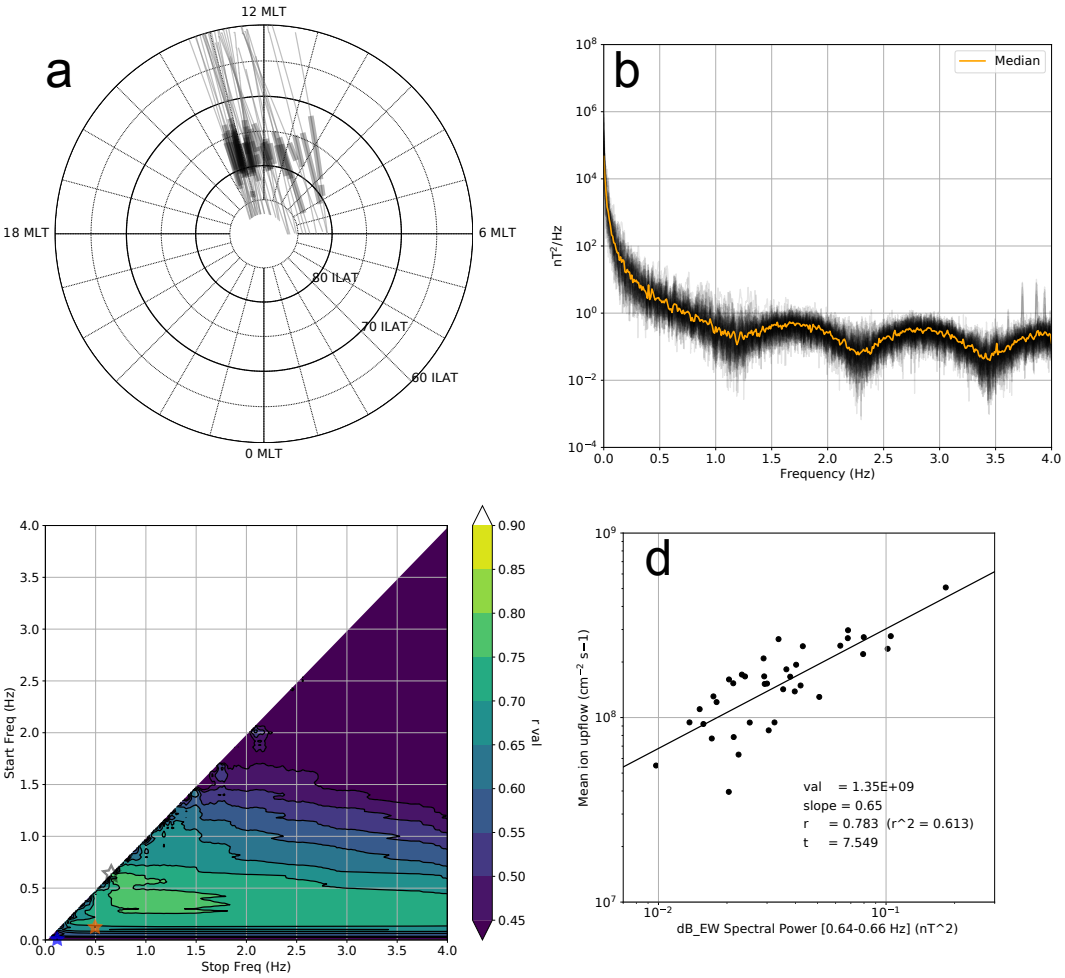

Figure 4. Ion and ΔB_{EW} statistics from 38 NH cusp-region passes between December 30, 1996 and January 7, 1997. The format of all panels is identical to corresponding panels in Figure 3. (a) Portions of orbits between 60–87° MLat, 6–18 MLT, and at or above 3800-km altitude. Thick lines indicate identified ion outflow. In panel d the spacecraft-frame frequency band that yields the highest correlation coefficient is 0.64–0.66 Hz.

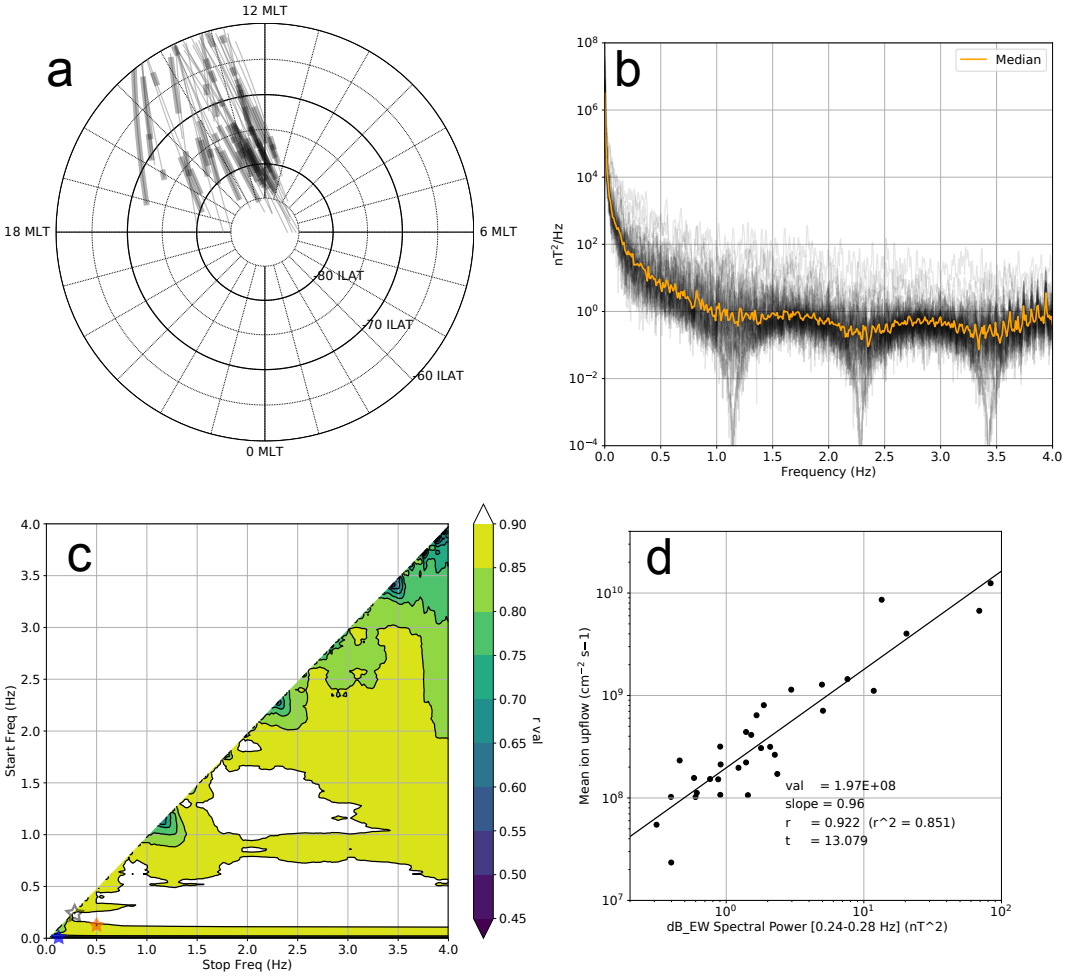

Figure 5. Ion and ΔB_{EW} statistics from 32 SH cusp-region passes during January 8–15, 1999. The format of all panels is identical to corresponding panels in Figure 3. (a) Portions of orbits between -87° and -60° MLat, 6–18 MLT, and at or above 3800-km altitude. Thick lines indicate identified ion outflow. In panel d the spacecraft-frame frequency band that yields the highest correlation coefficient is 0.24–0.28 Hz.

relatively smaller number of outflow observations made below these magnetic latitudes correspond to the portion of the 8-day observational period that coincides with a geomagnetic storm ($Dst_{\min} = -110$ nT) during January 13–17.

Figure 5b shows that the individual PSD estimates (transparent black lines) and median PSD (orange line) are comparable to the PSD estimates and median PSD shown in Figure 3b. The median PSD ranges over approximately seven orders of magnitude, and decreases by more than three orders of magnitude between 0 Hz and ∼0.2 Hz. Similar to the artifacts visible in Figure 3b, the spiked spectral features at $\gtrsim 3.5$ Hz are also artifacts related to the `ucla_mag_despin` routine. The troughs at ∼1.25 Hz, 2.35 Hz, and 3.45 Hz are related to the recursive filter of the fluxgate magnetometer.

In Figure 5c, the correlation coefficient $r \geq 0.85$ for approximately 90% of all spacecraft-frame frequency bands considered. Correlation coefficients $r \geq 0.90$ correspond to frequency bands given by either 1 Hz$\leq f_{\text{bot}} \leq$1.6 Hz and$f_{\text{bot}} \leq f_{\text{top}} \leq$2.6 Hz, or 0.1 Hz$\leq f_{\text{bot}} \leq$0.6 Hz and 0.2 Hz$\leq f_{\text{top}} \leq$4 Hz. In particular the spacecraft-frame frequency band 0.24–0.28 Hz yields the highest correlation coefficient $r = 0.922$, with a best-fit relationship $J_{\parallel,i} = 1.97 \times 10^8 P_{EW}^{0.96}$.

3.4 Southern Hemisphere, May 1998 (Late Local Fall)

Figure 6 shows the results of analysis of 19,800 frequency bands between 0 Hz and 4 Hz for 29 SH cusp-region passes occurring between May 24 and June 5, 1999, corresponding to late fall. The layout is identical to that of Figure 3. Figure 6a shows that ion outflows are mostly observed at MLat $\gtrsim 70°$ during these passes. The two regions of outflow over 14–15.5 MLT and near or below 70° MLat were observed during periods of weak geomagnetic activity ($Dst_{\min} = -34$ nT) that occurred intermittently during the 13-day observational period.

Figure 6b shows that the individual PSD estimates (transparent black lines) and median PSD (orange line) vary less overall than the PSD estimates shown in Figure 3b. The median PSD ranges over more than six orders of magnitude overall, and decreases by more than three orders of magnitude over 0–0.2 Hz. The two spikes that reach ∼10 nT^2/Hz at ∼3.7 Hz and 3.85 Hz are artifacts related to the `ucla_mag_despin` routine, whereas the deep troughs at ∼1.2 Hz, 2.35 Hz, and 3.45 Hz are related to the recursive filter of the fluxgate magnetometer.

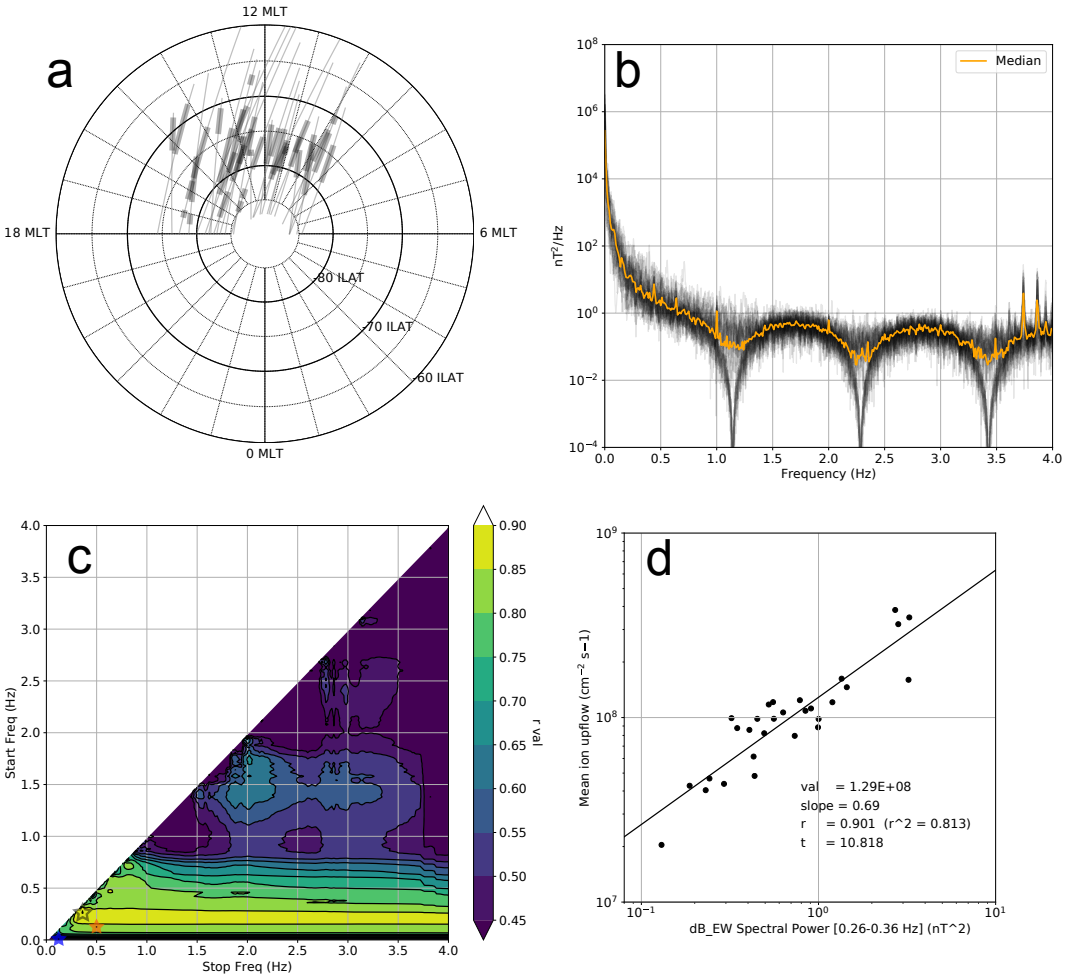

Figure 6. Ion and ΔB_{EW} statistics from 29 SH cusp-region passes between May 24 and June 5 in 1998. The format of all panels is identical to corresponding panels in Figure 3. (a) Portions of orbits between -87° and -60° MLat, 6–18 MLT, and at or above 3800-km altitude. Thick lines indicate identified ion outflow. In panel d the spacecraft-frame frequency band that yields the highest correlation coefficient is 0.26–0.36 Hz.

Figure 6c shows that the highest correlation coefficients ($r \geq 0.85$) correspond to spacecraft-frame frequency bands such that 0.2 Hz$\leq f_{\rm bot} \leq$0.4 Hz, 0.25 Hz$\leq f_{\rm top} \leq$4 Hz. The frequency band 0.26–0.36 Hz yields the highest correlation coefficient $r = 0.901$, with a best-fit relationship $J_{\parallel,i} = 1.29 \times 10^8 P_{EW}^{0.69}$.

4 Discussion and Summary

Two primary goals of this study are validation of the spectral method for studying the relationship between field fluctuations and upward ion fluxes, and expansion of the original data set considered by S05 and B11 to the Southern Hemisphere and other seasons. Results in Figures 2–6 demonstrate that empirical relationships very similar to those reported by S05 and B11 arise without inclusion of electric field measurements, and without recourse to visual determination of the cutoff energy (see sections 2.1 and 2.3). While we believe these aspects are significant, our methodology and data sets are nevertheless subject to their own limitations.

First, the algorithm for automated identification of ion outflows presented in section 2.1 is well suited to cusp-region energetic ion outflows, but likely misses other forms of energetic ion up/outflows that are more typical at other local times, such as nightside ion beams (Kondo et al., 1990). We have elsewhere developed and employed an algorithm for automated identification of ion beams (Hatch et al., 2018), which could be employed in possible future work dealing with the relationship between ion beams and field fluctuations.

Second, throughout this study we have relied on the assumption of S05 and B11 that the relationship between upward ion flux and field fluctuations is of the form of a power law. The scatter plots shown in b panels of Figures 2–6 provide clear evidence that such a relationship could be derived from first principles for the presented ranges of spectral powers and outflow fluxes, but leave as an open question whether a power-law relationship is valid for fluxes and spectral powers outside the observed ranges. Existing attempts in the literature (Horwitz & Zeng, 2009; Moore & Khazanov, 2010; Varney et al., 2016) to theoretically reproduce the observations presented by S05 and B11 represent important steps toward a full theoretical description, but each study points to a need for more observational data.

Third, regarding field measurements, we have not used FAST electric field measurements to estimate the field-aligned Poynting flux, as did S05 and B11. Our approach thus lacks information about input wave energies. On the other hand this approach opens the exploitation of magnetic field measurements as a possibly powerful alternative to Poynting flux measurements in studies of energetic ion outflows, and could yield a significant contribution to filling the knowledge gaps mentioned in the Introduction. This approach is the planned subject of future work.

Fourth, we have exclusively considered the east-west component of the measured magnetic field. This component yields overall higher correlation coefficients than those yielded when we instead use the north-south component of the measured magnetic field, though in many cases the differences are slight. Our choice is also motivated by the preferential east-west orientation of Alfvénic magnetic field perturbations, as already discussed in the Introduction (section 1).

We believe that a critical aspect of this study is the stringent criteria on spacecraft MLT, Mlat, altitude, and direction of approach to the cusp region. We have discussed in section 2 that the purpose of these criteria is to reduce potential Doppler shifting of field measurements and to exclude ram ions as much as possible. With these criteria there emerges from the analysis of each group of orbits some common characteristics of the relationship between ion outflows and east-west magnetic field fluctuations, which we now discuss. (Text S1 and Figures S1–S4 in the Supporting Information provides versions of the analysis in Figures 3–6 with the restriction to altitudes of 3800 km or greater relaxed.)

The most salient feature in panel c for each of Figures 3–6 in section 3 is that the correlation between ion outflows and east-west magnetic field fluctuations ΔB_{EW} is highest for spacecraft-frame frequencies $f_{sc} \lesssim 0.7$ Hz. Only orbits in Group 2 (section 3.2) involve pole-to-equator traversals of the cusp region, and as we discuss below in connection with Table 3, Group 2 spacecraft-frame frequency bands may be Doppler-shifted by as much as 40% relative to the three groups of orbits for which FAST approaches the cusp region from the equator. For these other three groups of orbits the upper limit of frequencies corresponding to high correlations is accordingly even narrower, $f_{sc} \lesssim 0.4$ Hz.

Regardless of the direction of approach, panel c for each of Figures 3–6 shows that the degree of correlation r varies primarily with the the lower bound $f_{\rm bot}$ (y axis) of a given frequency band, while the dependence on the upper bound $f_{\rm top}$ (x axis) is rela-

Table 2. Best-fit relationships for the frequency band 0.18–0.8 Hz.

Group	Section	Time period	Hemisphere	$J_{\parallel,i} = J_{0,i} P_{EW}^{\gamma}$ $(J_{0,i},\, \gamma)^*$	r	$\langle F10.7 \rangle_{27}{}^{\dagger}$ $10^{-22}\mathrm{J/m^2}$
1	3.1	September 1998	Northern	$\left(10^{7.055}, 1.166\right)$	0.926	144–146
2	3.2	December 1996	Northern	$\left(10^{7.776}, 0.703\right)$	0.744	75–76
3	3.3	January 1999	Southern	$\left(10^{7.444}, 0.991\right)$	0.916	137–143
4	3.4	May 1998	Southern	$\left(10^{7.622}, 0.792\right)$	0.873	105–111

$^*J_{0,i}$ is the mapped upward ion flux (in $\mathrm{cm^{-2}s^{-1}}$) for nominal spectral power $P_{EW} = 1\ \mathrm{nT^2}$. P_{EW} is the integral of the ΔB_{EW} PSD (in $\mathrm{nT^2/Hz}$) over 0.18–0.8 Hz.

†The angle brackets $\langle\rangle_{27}$ denote a backwards-looking average over a 27-day window.

tively much weaker. The dominating role of f_{bot} in the variation of the correlation coefficient arises due to the general shape of the PSD estimates corresponding to each orbit (transparent black lines in panel b for each of Figures 3–6). Each PSD estimate exhibits a logarithmic, and approximately monotonic, decrease with increasing frequency up to $f_{sc} \sim 1$ Hz. Thus the spectral power P_{EW} obtained from integration of any frequency band with a lower bound $f_{bot} \leq 1$ Hz is primarily determined by f_{bot} and largely invariant with respect to the upper bound f_{top}.

To make the results shown in Figures 3–6 easily implementable for modellers, Table 2 provides best-fit relationships of the form $J_{\parallel,i} = J_{0,i} P_{EW}^{\gamma}$ between upward ion flux mapped to 130-km altitude $J_{\parallel,i}$, spectral power P_{EW}, and power-law index $\gamma \simeq 0.7$–1.2 for the spacecraft-frame frequency band 0.18–0.8 Hz. We have chosen this frequency band because it yields the "maximum average correlation coefficient" $\bar{r}_{\mathrm{max}}$ obtained as follows.

Let $r_i(f_{\mathrm{bot}}, f_{\mathrm{top}})$ be the correlation coefficient for the ith orbit group, where $i \in (0, 1, 2, 3)$ indicates one of the four groups of orbits in Tables 1 and 2, and $(f_{\mathrm{bot}}, f_{\mathrm{top}})$ denotes any of the 19,800 frequency bands represented by the x and y axes of panel c in Figures 3–6. Then the "maximum average correlation coefficient" $\bar{r}_{\mathrm{max}} = \max(r_A)$ $= \max(\frac{1}{4}\sum_i r_i(f_{\mathrm{bot}}, f_{\mathrm{top}})) = 0.865$ is obtained for the frequency band ($f_{\mathrm{bot}} = 0.18$ Hz, $f_{\mathrm{top}} = 0.8$ Hz). This frequency band also yields the maximum if we instead calculate the maximum via the geometric mean or the harmonic mean.

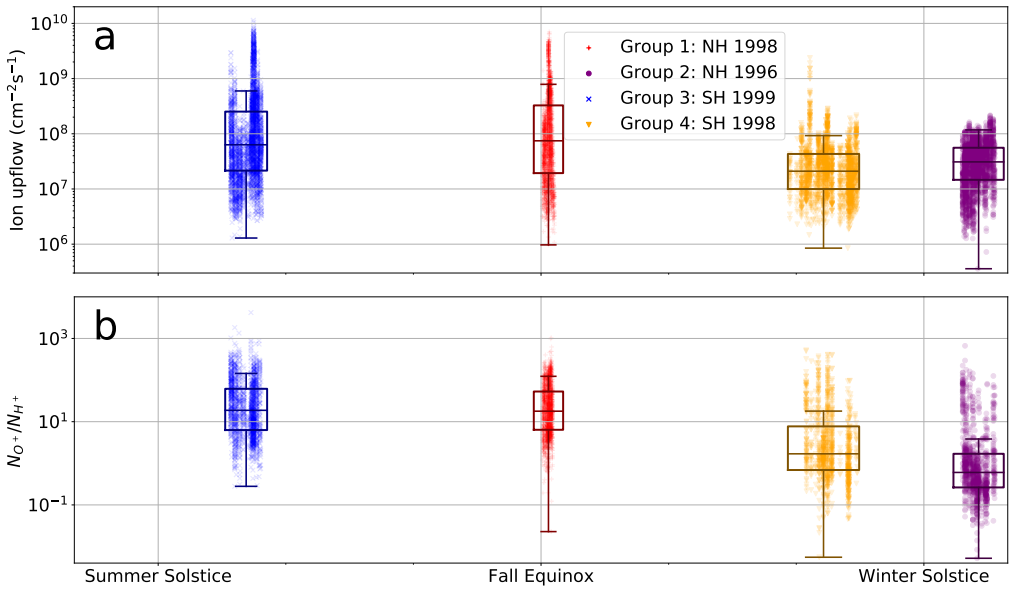

Figure 7. (a) Scatterplots of observed upward ion fluxes for each of the four groups of orbits analyzed in section 3 and indicated in Tables 1–3, as a function of season. (b) O^+/H^+ density ratios derived from TEAMS mass spectrometer measurements for 114 of the 132 orbits shown in panel a (see text). In both panels a box plot is shown for each orbit group to indicate the median as well as upper and lower quartiles Q3 and Q1. The top and bottom lines for each box plot respectively indicate the values Q3 + 1.5IQR and Q1 − 1.5IQR, with IQR≡Q3−Q1.

Figure 7a shows, for all 132 orbits used in this study, individually observed ion outflow fluxes (mapped to 130-km altitude) as a function of season. Group 1 and Group 3 upward ion fluxes (red plus and blue x symbols), which respectively occurred near fall equinox and summer solstice, are overall greater than Group 2 and Group 4 upward ion fluxes (purple circle and orange triangle symbols), which both occurred near winter solstice. This observation leads us to consider the dependence of upward ion fluxes on season.

Two causes of long-term variation in the properties of outflowing ions are season and solar cycle. On point of season, Yau et al. (1985) found that the occurrence of O^+ upflows over altitudes of 8,000 to 23,000 km is favored by summer solstice, while they found no significant variation of the occurrence of H^+ with season. On point of solar cycle, Yau et al. (1988) found that the outflowing O^+/H^+ ratio increases by an order of magnitude from solar minimum to solar maximum.

Group 1 orbits (Sep 23–26 1998) occurred near fall equinox during which 27-day-averaged F10.7 indices $\langle F_{10.7} \rangle_{27} = 144$–$146$, the highest F10.7 range for all four orbit groups (rightmost column in Table 2; F10.7 values were obtained from `https://omniweb.gsfc.nasa.gov/form/dx1.html`). Group 2 orbits (Dec 30 1996 to Jan 7 1997) occurred near local winter, during which $\langle F_{10.7} \rangle_{27} = 75$–$76$ (i.e., near solar minimum), the lowest range of $\langle F_{10.7} \rangle_{27}$ values for all four orbit groups. Based on the higher range of $\langle F_{10.7} \rangle_{27}$ values observed during Group 1 orbits, we expect that Group 1 outflows are relatively much richer in O^+ than Group 2 outflows.

Group 3 orbits (Jan 8–15 1999) occurred near summer solstice with $\langle F_{10.7} \rangle_{27} = 137$–$143$, only slightly lower than the Orbit Group 1 $\langle F_{10.7} \rangle_{27}$ range. Group 4 orbits (May 24 to Jun 5 1998) occurred near winter solstice with $\langle F_{10.7} \rangle_{27} = 105$–$111$, intermediate to the $\langle F_{10.7} \rangle_{27}$ ranges for the other three orbit groups.

Based on these differences in season and solar cycle for the four groups of orbits, we expect that Group 1 and Group 3 outflows are richest in O^+, with Group 4 outflows somewhat poorer and Group 2 outflows poorest in O^+. To directly demonstrate the existence of these differences, Figure 7b shows the O^+/H^+ density ratio derived from analysis of ion composition measurements made by the Time-of-Flight Energy, Angle, Mass Spectrograph (TEAMS) instrument (Klumpar et al., 2001) aboard FAST. As with upward ion fluxes in panel a, each data point represents an individual O^+/H^+ density ra-

tio estimate for TEAMS observations made during 114 of the 132 orbits shown in Figure 7a. (TEAMS measurements were unavailable for the other 18 passes.) The density moment is calculated for each species distribution function measured by TEAMS by integrating over all angles, and from 4 eV up to the IESA energy cutoff E_{top} given by the outflow identification algorithm in section 2.1. (For example, E_{top} is indicated by the pink line in Figure 1d.) Each TEAMS measurement is required to meet the same criteria from section 2 that we have applied to FAST IESA and magnetometer data, and we include only those TEAMS measurements that correspond to time periods when ion outflow is positively identified in IESA measurements.

Figure 7b reveals that the upflows observed near or during summer solstice are relatively much richer in O^+ than those during winter, as expected. Thus the overall lower upward fluxes in and near wintertime in Figure 7 may be related to the lower fraction of O^+ present during winter solstice and during periods of lower solar activity.

TEAMS measurements are currently undergoing additional calibration and deadtime correction by a study coauthor (E. J. Lund). At present these measurements likely underestimate the actual densities of each species and are not suitable for the correlation analysis that we have performed in section 3. But the overall trends and order-of-magnitude differences are sufficient to underscore that the composition of ionospheric outflow likely play a role in seasonal variations of the relationship between ionospheric outflow and magnetic field perturbations that we have demonstrated. Thus Figure 7 demonstrates that ion composition should not be neglected in any comprehensive model of wave-driven energetic ion outflows. Although outside the scope of this study, we reserve extended treatment of ion composition as a possible focus of future work.

Returning to the question of Doppler shifting raised in section 2 and at the beginning of this section, we now show that the assumptions

1. field variations observed by FAST over 0–4 Hz in the spacecraft frame of reference are spatial and not temporal ($\omega(\mathbf{k}) = 0$);
2. the variation of magnetic field perturbations is primarily perpendicular to the background magnetic field (i.e., $k_\perp \gg k_\parallel$);

Table 3. Estimated transverse spatial scales $L_\perp$ corresponding to ion outflow[a]

Group	Section	Time period	Hemisphere	$r_{90\%}$[b]	f_{bot} range[c] (Hz)	$\mid v_{F,\perp} - V \mid$ (km/s)	$L_\perp^d$ (km)
1	3.1	September 1998	Northern	0.91	0.04–0.26	4.5	17–110
2	3.2	December 1996	Northern	0.74	0.15–0.64	6.5	10–42
3	3.3	January 1999	Southern	0.91	0.13–0.28	4.5	16–35
4	3.4	May 1998	Southern	0.83	0.09–0.34	4.5	13–49

[a]Via equation (3), which assumes observed B-field variations are purely spatial.

[b]For each orbit group, the lower bound of the highest 10% of all calculated r values.

[c]Approximate range of "start frequencies" f_{bot} for which correlation coefficient $r \geq r_{90\%}$.

[d]Perpendicular scale size near FAST apogee at ∼4100-km altitude.

appear consistent with the results shown in panels c of Figures 3–6. With these assumptions the observed spacecraft-frame frequencies arise via Doppler shifting according to

$$\omega_{\rm sc}(\mathbf{k}) = 2\pi f_{\rm sc}(\mathbf{k}) = \mid \mathbf{k} \cdot (\mathbf{v}_F - \mathbf{V}) \mid \approx \mid k_\perp \, (v_{F,\perp} - V) \mid, \tag{2}$$

where $v_{F,\perp}$ is the perpendicular speed of FAST and V is the poleward plasma convection speed. Thus the spacecraft-frame frequency f_{sc} corresponds to a perpendicular spatial scale

$$L_\perp = \frac{\mid v_{F,\perp} - V \mid}{f_{sc}}. \tag{3}$$

Typical convection speeds in the dayside cusp region range from hundreds of m/s up to 2–3 km/s during active conditions (Moen et al., 1996; Skjæveland et al., 2011, 2014), and typical speeds of FAST perpendicular to the background magnetic field at apogee are $\mid v_{F,\perp} \mid$=5.2–5.6 km/s.

We assume V =1 km/s and $v_{F,\perp} = \pm 5.5$ km/s, where the positive sign corresponds to poleward orbits (i.e., Groups 1, 3, and 4) and the negative sign corresponds to equatorward orbits (i.e., Group 2). We then apply equation (3) to the range of "start frequencies" f_{bot}, indicated on the y axis of panel c for Figures 3–6, for which $r \geq r_{90\%}$. (The subscript "0.9" denotes the 0.9 quantile of all calculated r values for a particular orbit group. For example, 10% of all r values in Figure 3c are 0.91 or greater; thus $r_{90\%}$ = 0.91 in Table 3.)

The rightmost column of Table 3 shows the resulting range of perpendicular spatial scales at FAST apogee for each group of orbits. If the above-stated assumptions are valid, east-west field variations with perpendicular spatial scales of order tens of kilometers are associated with ion outflow.

As a consistency check, applying equation 2 to the range of scale sizes $L_\perp$ = 10–42 km corresponding to Group 2 in Table 3 shows that if FAST had been moving poleward instead of equatorward in the presence of plasma convecting poleward at 1 km/s, these scale sizes would have been observed over the space-craft frequency range f_{bot} =0.11–0.44 Hz. Though not proof, that this range is more consistent with the f_{bot} ranges for Groups 1, 3, and 4 in Table 3 suggests the above assumptions are at least plausible.

These perpendicular scales are in between large scales (of order hundreds or thousands of kilometers, corresponding to quasistatic field-aligned currents and the electrojets) and kinetic scales (of order 1 m to a few km, corresponding to local ion gyroradii and the electron inertial length) within and in the vicinity of the dayside cusp. Thus, instead of corresponding to direct driving of energetic ion outflow, these scales may be related to a number of processes that are associated with ion outflow.

Both simulations (Génot et al., 2004; Chaston et al., 2004; Rankin et al., 2005) and satellite observations (Chaston et al., 2006) have shown that the interaction of shear Alfvén waves with a preexisting ionospheric density irregularity produces field-aligned broadband electron precipitation, transverse ion acceleration, ion heating and plasma depletion (Chaston et al., 2006, Figure 6). This interaction also leads to phase mixing and the production of field fluctuations over perpendicular scales ranging from the scale size of the density irregularity down to and below the electron inertial length, typically of order km in the magnetosphere-ionosphere transition region.

As observed by Lotko and Zhang (2018), evidence that these perpendicular spatial scales are associated with Alfvén waves has been reported by Ishii et al. (1992). Using DE-2 measurements at 300-km altitude they showed that field perturbations over DE-2 spacecraft-frame frequencies of $\gtrsim$ 0.25 Hz were more consistent with an Alfvénic rather than a quasistatic interpretation; treating this frequency range as resulting from Doppler-shifted spatial structures, they reported perpendicular spatial scales of $\lesssim$30 km at 300-km altitude ($\lesssim$60 km near FAST apogee).

In conclusion, in this study we have validated and applied a new methodology for examining the relationship between ion outflows and field fluctuations in the dayside cusp-region in both hemispheres and as a functon of season. We have presented an algorithm that achieves automated identification of ionospheric-origin ion outflows, and a spectral method for analysis of the relationship between these outflows and east-west magnetic field perturbations over nearly arbitrary frequency bands. Using four groups of orbits, two from each hemisphere, we have found that field perturbations over spacecraft-frame frequencies of less than 0.7 Hz show the highest correlation with cusp-region ion outflows. Best-fit relationships between these field perturbations and ion outflows yield power-law indices between 0.7 and 1.2, where the lowest power-law values are associated with winter/late fall and the highest values associated with fall equinox/summer. Previous studies indicate that fluctuations over these frequency ranges are likely associated with Alfvén waves. If the observed perturbations are primarily spatial in nature, they correspond to perpendicular scale sizes of several to tens of kilometers.

We have also demonstrated that ion composition likely plays a significant role in the relationship between ionospheric-origin energetic outflows and field fluctuations. This study underscores the need for much larger ion outflow data sets made up of observations for which the effects of ram ions and Doppler shifting due to spacecraft motion are consistently accounted for or otherwise mitigated.

Acknowledgments

All observations and measurements made by the FAST spacecraft are available as a Level 1 data product through SDT. Work at the Birkeland Center for Space Science and the University of Bergen was funded by the Research Council of Norway/CoE under contract 223252/F50 and by ESA contract 4000126731 in the framework of EO Science for Society. Work at the University of New Hampshire is supported by the National Science Foundation under grant 1502937. S. M. Hatch thanks J. Bonnell, M. Burleigh, C. Chaston, and A. Yau for helpful commentary and feedback on the draft manuscript of this study.

References

Brambles, O. J., Lotko, W., Damiano, P. a., Zhang, B., Wiltberger, M., & Lyon,

J. (2010). Effects of causally driven cusp O+ outflow on the storm time magnetosphere-ionosphere system using a multifluid global simulation. *Journal of Geophysical Research: Space Physics*, *115*(9), 1–14. doi: 10.1029/2010JA015469

Brambles, O. J., Lotko, W., Zhang, B., Wiltberger, M., Lyon, J., & Strangeway, R. J. (2011). Magnetosphere sawtooth oscillations induced by ionospheric outflow. *Science*, *332*(6034), 1183–1186. doi: 10.1126/science.1202869

Burchill, J. K., Knudsen, D. J., Clemmons, J. H., Oksavik, K., Pfaff, R. F., Steigies, C. T., ... Yeoman, T. K. (2010). Thermal ion upflow in the cusp ionosphere and its dependence on soft electron energy flux. *Journal of Geophysical Research*, *115*, 1–16. doi: 10.1029/2009JA015006

Carlson, C. W., Mcfadden, J. P., Turin, P., Curtis, D. W., & Magoncelli, A. (2001). The electron and ion plasma experiment for FAST. *Space Science Reviews*, *98*(1), 33–66. Retrieved from `http://dx.doi.org/10.1023/A:1013139910140` doi: 10.1023/A:1013139910140

Chaston, C. C., Bonnell, J. W., Carlson, C. W., McFadden, J. P., Ergun, R. E., & Strangeway, R. J. (2003). Properties of small-scale Alfvén waves and accelerated electrons from FAST. *Journal of Geophysical Research: Space Physics*, *108*(A4), 1–16. doi: 10.1029/2002JA009420

Chaston, C. C., Bonnell, J. W., Carlson, C. W., Mcfadden, J. P., Ergun, R. E., Strangeway, R. J., & Lund, E. J. (2004). Auroral ion acceleration in dispersive Alfven waves. , *109*, A04205. doi: 10.1029/2003JA010053

Chaston, C. C., Carlson, C. W., McFadden, J. P., Ergun, R. E., & Strangeway, R. J. (2007). How important are dispersive Alfvén waves for auroral particle acceleration? *Geophysical Research Letters*, *34*, L07101. doi: 10.1029/2006GL029144

Chaston, C. C., Genot, V., Bonnell, J. W., Carlson, C. W., McFadden, J. P., Ergun, R. E., ... Hwang, K. J. (2006). Ionospheric erosion by Alfvén waves. *Journal of Geophysical Research*, *111*(A3), A03206. Retrieved from `http://doi.wiley.com/10.1029/2005JA011367` doi: 10.1029/2005JA011367

Elphic, R. C., Means, J. D., Snare, R. C., Strangeway, R. J., Kepko, L., & Ergun, R. E. (2001). Magnetic field instruments for the Fast Auroral Snapshot explorer. *Space Science Reviews*, *98*, 151-168. doi: 10.1023/A:1013153623344

Ergun, R. E., Carlson, C. W., Mozer, F. S., Delory, G. T., Temerin, M., Mcfadden, J. P., ... Cattell, C. A. (2001). The Fast Satellite Fields Instrument. *Space Science Reviews*, *98*(1-2), 67–91. doi: 10.1023/A:1013131708323

Génot, V., Louarn, P., & Mottez, F. (2004). Alfvén wave interaction with inhomogeneous plasmas: acceleration and energy cascade towards small-scales. *Annales Geophysicae*, *22*(6), 2081–2096. Retrieved from `http://www.ann-geophys.net/22/2081/2004/` doi: 10.5194/angeo-22-2081-2004

Hatch, S. M., Chaston, C. C., & LaBelle, J. (2018, aug). Nonthermal limit of monoenergetic precipitation in the auroral acceleration region. *Geophysical Research Letters*, *45*(19), 10167–10176. Retrieved from `https://doi.org/10.1029/2018GL078948http://doi.wiley.com/10.1029/2018GL078948` doi: 10.1029/2018GL078948

Hatch, S. M., & LaBelle, J. (2018). Application of a new method for calculation of low-frequency wave vectors. In G. Fischer, G. Mann, M. Panchenko, & P. Zarka (Eds.), *Planetary radio emissions viii* (pp. 247–260). Vienna: Austrian Academy of Sciences Press. Retrieved from `https://hw.oeaw.ac.at?arp=0x0039b715` doi: 10.1553/PRE8s247

Hatch, S. M., Labelle, J., Lotko, W., Chaston, C. C., & Zhang, B. (2017). IMF control of Alfvénic energy transport and deposition at high latitudes. *Journal of Geophysical Research: Space Physics*, *122*(12). Retrieved from `http://dx.doi.org/10.1002/2017JA024175` doi: 10.1002/2017JA024175

Heelis, R. A., & Hanson, W. B. (1998, jan). *Measurements of Thermal Ion Drift Velocity and Temperature Using Planar Sensors.* Retrieved from `https://doi.org/10.1029/GM102p0061` doi: doi:10.1029/GM102p0061

Horwitz, J. L., & Zeng, W. (2009). Physics-based formula representations of high-latitude ionospheric outflows : H + and O + densities , flow velocities , and temperatures versus soft electron precipitation , wave-driven transverse heating , and solar zenith angle effects. *Journal of Geophysical Research*, *114*, 1–14. doi: 10.1029/2008JA013595

Howarth, A., & Yau, A. W. (2008, dec). The effects of IMF and convection on thermal ion outflow in magnetosphere-ionosphere coupling. *Journal of Atmospheric and Solar-Terrestrial Physics*, *70*(17), 2132–2143. Retrieved from `http://www.sciencedirect.com/science/article/pii/S1364682608002241`

doi: 10.1016/j.jastp.2008.08.008

Ishii, M., Sugiura, M., Iyemori, T., & Slavin, J. A. (1992, sep). Correlation between magnetic and electric field perturbations in the field-aligned current regions deduced from DE 2 observations. *Journal of Geophysical Research: Space Physics*, *97*(A9), 13877–13887. Retrieved from https://doi.org/10.1029/92JA00110 doi: 10.1029/92JA00110

Kervalishvili, G. N., & Lühr, H. (2013, mar). The relationship of thermospheric density anomaly with electron temperature, small-scale FAC, and ion up-flow in the cusp region, as observed by CHAMP and DMSP satellites. *Annales Geophysicae*, *31*(3), 541–554. Retrieved from http://www.ann-geophys.net/31/541/2013/http://www.ann-geophys.net/31/541/2013/angeo-31-541-2013.pdf doi: 10.5194/angeo-31-541-2013

Klumpar, D. M., Möbius, E., Kistler, L. M., Popecki, M., Hertzberg, E., Crocker, K., ... Hovestadt, D. (2001). The Time-of-Flight Energy, Angle, Mass Spectrograph (TEAMS) experiment for FAST. *Space Science Reviews*, *98*(1), 197–219. Retrieved from https://doi.org/10.1023/A:1013127607414 doi: 10.1023/A:1013127607414

Kondo, T., Whalen, B. A., Yau, A. W., & Peterson, W. K. (1990, aug). Statistical analysis of upflowing ion beam and conic distributions at DE 1 altitudes. *Journal of Geophysical Research: Space Physics*, *95*(A8), 12091–12102. Retrieved from https://doi.org/10.1029/JA095iA08p12091 doi: 10.1029/JA095iA08p12091

Laundal, K. M., & Richmond, A. D. (2016). Magnetic Coordinate Systems. *Space Science Reviews*, 1–33. Retrieved from http://dx.doi.org/10.1007/s11214-016-0275-y doi: 10.1007/s11214-016-0275-y

Lee, S. H., Zhang, H., Zong, Q.-G., Otto, A., Rème, H., & Liebert, E. (2016, jan). A statistical study of plasmaspheric plumes and ionospheric outflows observed at the dayside magnetopause. *Journal of Geophysical Research: Space Physics*, *121*(1), 492–506. Retrieved from http://doi.wiley.com/10.1002/2015JA021540 doi: 10.1002/2015JA021540

Lotko, W., & Zhang, B. (2018, dec). Alfvénic Heating in the Cusp Ionosphere-Thermosphere. *Journal of Geophysical Research: Space Physics*, *0*(0). Retrieved from https://doi.org/10.1029/2018JA025990 doi: 10.1029/

652 2018JA025990

653 Moen, J., Lockwood, M., Sandholt, P. E., Løvhaug, U. P., Denig, W. F., van
654 Eyken, A. P., & Egeland, A. (1996). Variability of dayside high lati-
655 tude convection associated with a sequence of auroral transients. *Jour-*
656 *nal of Atmospheric and Terrestrial Physics*, *58*(1), 85–96. Retrieved from
657 http://www.sciencedirect.com/science/article/pii/0021916995000216
658 doi: https://doi.org/10.1016/0021-9169(95)00021-6

659 Moore, T. E., Fok, M.-C., Delcourt, D. C., Slinker, S. P., & Fedder, J. A. (2007).
660 Global aspects of solar wind–ionosphere interactions. *Journal of Atmo-*
661 *spheric and Solar-Terrestrial Physics*, *69*(3), 265–278. Retrieved from
662 http://www.sciencedirect.com/science/article/pii/S1364682606002665
663 doi: https://doi.org/10.1016/j.jastp.2006.08.009

664 Moore, T. E., & Horwitz, J. L. (2007). Stellar ablation of planetary atmospheres.
665 *Reviews of Geophysics*, *45*(3), 1–34. doi: 10.1029/2005RG000194

666 Moore, T. E., & Khazanov, G. V. (2010, dec). Mechanisms of ionospheric mass es-
667 cape. *Journal of Geophysical Research: Space Physics*, *115*(A12). Retrieved
668 from https://doi.org/10.1029/2009JA014905 doi: 10.1029/2009JA014905

669 Moore, T. E., Pollock, C. J., & Young, D. T. (1998, mar). Kinetic Core Plasma
670 Diagnostics. In *Measurement techniques in space plasmas:particles* (pp. 105–
671 123). American Geophysical Union. Retrieved from http://dx.doi.org/
672 10.1029/GM102p0105http://doi.wiley.com/10.1029/GM102p0105 doi: 10
673 .1029/GM102p0105

674 Norqvist, P., André, M., & Tyrland, M. (1998, oct). A statistical study of
675 ion energization mechanisms in the auroral region. *Journal of Geophys-*
676 *ical Research: Space Physics*, *103*(A10), 23459–23473. Retrieved from
677 http://doi.wiley.com/10.1029/98JA02076 doi: 10.1029/98JA02076

678 Peterson, W. K., Andersson, L., Callahan, B., Elkington, S. R., Winglee, R. W.,
679 Scudder, J. D., & Collin, H. L. (2008, nov). Geomagnetic activity de-
680 pendence of O+ in transit from the ionosphere. *Journal of Atmospheric*
681 *and Solar-Terrestrial Physics*, *71*(16), 1623–1629. Retrieved from http://
682 www.sciencedirect.com/science/article/pii/S1364682608003684 doi:
683 10.1016/j.jastp.2008.11.003

684 Rankin, R., Marchand, R., Lu, J. Y., Kabin, K., & Tikhonchuk, V. T. (2005, mar).

Theory of dispersive shear Alfvén wave focusing in Earth's magnetosphere. *Geophysical Research Letters*, *32*(5). Retrieved from https://doi.org/10.1029/2004GL021831 doi: 10.1029/2004GL021831

Richmond, A. D. (1995). Ionospheric Electrodynamics Using Magnetic Apex Coordinates. *Journal of geomagnetism and geoelectricity*, *47*(2), 191–212. doi: 10.5636/jgg.47.191

Skjæveland, Å., Moen, J., & Carlson, H. C. (2011, oct). On the relationship between flux transfer events, temperature enhancements, and ion upflow events in the cusp ionosphere. *Journal of Geophysical Research*, *116*(A10), A10305. Retrieved from http://doi.wiley.com/10.1029/2011JA016480 doi: 10.1029/2011JA016480

Skjæveland, Å., Moen, J., & Carlson, H. C. (2014, aug). Which cusp upflow events can possibly turn into outflows? *Journal of Geophysical Research: Space Physics*, *119*(8), 6876–6890. Retrieved from http://doi.wiley.com/10.1002/2013JA019495 doi: 10.1002/2013JA019495

Slepian, D. (1978, may). Prolate Spheroidal Wave Functions, Fourier Analysis, and Uncertainty—V: The Discrete Case. *Bell System Technical Journal*, *57*(5), 1371–1430. Retrieved from http://dx.doi.org/10.1002/j.1538-7305.1978.tb02104.x doi: 10.1002/j.1538-7305.1978.tb02104.x

Stasiewicz, K., Bellan, P., Chaston, C., Kletzing, C., Lysak, R., Maggs, J., ... Wahlund, J.-E. (2000). Small scale Alfvenic Structure in the Aurora. *Space Science Reviews*, *92*(3–4), 423–533. doi: 10.1023/A:1005207202143

Strangeway, R. J., Ergun, R. E., Su, Y., Carlson, C. W., & Elphic, R. C. (2005). Factors controlling ionospheric outflows as observed at intermediate altitudes. *Journal of Geophysical Research: Space Physics*, *110*, A03221. doi: 10.1029/2004JA010829

Su, Y.-J., Caton, R. G., Horwitz, J. L., & Richards, P. G. (1999, jan). Systematic modeling of soft-electron precipitation effects on high-latitude F region and topside ionospheric upflows. *Journal of Geophysical Research: Space Physics*, *104*(A1), 153–163. Retrieved from https://doi.org/10.1029/1998JA900068http://doi.wiley.com/10.1029/1998JA900068 doi: 10.1029/1998JA900068

Thomson, D. (1982). Spectrum estimation and harmonic analysis. *Proceedings of*

the IEEE, *70*(9), 1055–1096. Retrieved from http://ieeexplore.ieee.org/document/1456701/ doi: 10.1109/PROC.1982.12433

van der Meeren, C., Burrell, A. G., & Laundal, K. M. (2018). *apexpy: Apexpy version 1.0.3.* http://doi.org/10.5281/zenodo.1214207.

Varney, R. H., Wiltberger, M., Zhang, B., Lotko, W., & Lyon, J. (2016, oct). Influence of ion outflow in coupled geospace simulations: 1. Physics-based ion outflow model development and sensitivity study. *Journal of Geophysical Research: Space Physics*, *121*(10), 9671–9687. Retrieved from http://dx.doi.org/10.1002/2016JA022777 doi: 10.1002/2016JA022777

Welling, D. T., André, M., Dandouras, I., Delcourt, D., Fazakerley, A., Fontaine, D., ... Yau, A. (2015). The Earth: Plasma Sources, Losses, and Transport Processes. *Space Science Reviews*, *192*, 145–208. Retrieved from http://link.springer.com/10.1007/s11214-015-0187-2 doi: 10.1007/s11214-015-0187-2

Wilson, G. R., Ober, D. M., Germany, G. A., & Lund, E. J. (2004). Nightside auroral zone and polar cap ion outflow as a function of substorm size and phase. *Journal of Geophysical Research*, *109*(A02206), 1–18. doi: 10.1029/2003JA009835

Yau, A. W., & André, M. (1997). Sources of Ion Outflow in the High Latitude Ionosphere. *Space Science Reviews*, *80*, 1–25.

Yau, A. W., Beckwith, P. H., Peterson, W. K., & Shelley, E. G. (1985, jul). Long-term (solar cycle) and seasonal variations of upflowing ionospheric ion events at DE 1 altitudes. *Journal of Geophysical Research: Space Physics*, *90*(A7), 6395–6407. Retrieved from https://doi.org/10.1029/JA090iA07p06395 doi: 10.1029/JA090iA07p06395

Yau, A. W., Peterson, W. K., & Shelley, E. G. (1988, jan). Quantitative parametrization of energetic ionospheric ion outflow. In *Modeling magnetospheric plasma* (Vol. 44, pp. 211–217). American Geophysical Union. Retrieved from http://dx.doi.org/10.1029/GM044p0211https://doi.org/10.1029/GM044p0211 doi: doi:10.1029/GM044p0211

Zhang, B., Brambles, O., Lotko, W., Smith, R., Wiltberger, M., & Lyon, J. (2013). Predicting the Location of Polar Cusp in the Lyon-Fedder-Mobarry global magnetosphere simulation. *Journal of Geophysical Research*. doi:

10.1002/jgra.50565

Zhang, B., Lotko, W., Brambles, O., Xi, S., Wiltberger, M., & Lyon, J. (2014, mar). Solar wind control of auroral Alfvénic power generated in the magnetotail. *Journal of Geophysical Research: Space Physics*, *119*(3), 1734–1748. Retrieved from u doi: 10.1002/2013JA019178

Zhang, Q.-H., Zong, Q.-G., Lockwood, M., Heelis, R. A., Hairston, M., Liang, J., ... Ma, Y.-Z. (2016, feb). Earth's ion upflow associated with polar cap patches: Global and in situ observations. *Geophysical Research Letters*, *43*(5), 1845–1853. Retrieved from https://doi.org/10.1002/2016GL067897 doi: 10.1002/2016GL067897

Zheng, Y., Moore, T. E., Mozer, F. S., Russell, C. T., & Strangeway, R. J. (2005, jul). Polar study of ionospheric ion outflow versus energy input. *Journal of Geophysical Research: Space Physics*, *110*(A7). Retrieved from https://doi.org/10.1029/2004JA010995 doi: 10.1029/2004JA010995

Zhou, X. W., Russell, C. T., Le, G., Fuselier, S. A., & Scudder, J. D. (2000). Solar wind control of the polar cusp at high altitude. *Journal of Geophysical Research*, *105*(A1), 245. Retrieved from http://www.agu.org/pubs/crossref/2000/1999JA900412.shtml doi: 10.1029/1999JA900412